

Temporally multimode four-photon Hong-Ou-Mandel interference

A. Ferreri , V. Ansari, C. Silberhorn, and P. R. Sharapova

Department of Physics, Paderborn University, Warburger Strasse 100, D-33098 Paderborn, Germany



(Received 3 May 2019; published 14 November 2019)

The two-photon Hong-Ou-Mandel (HOM) interference is a pure quantum effect which indicates the degree of indistinguishability of photons. The four-photon HOM interference exhibits richer dynamics in comparison to the two-photon interference and simultaneously is more sensitive to the input photon states. We demonstrate theoretically and experimentally an explicit dependency of the four-photon interference on the number of temporal modes, created in the process of parametric down-conversion. Moreover, we exploit the splitting ratio of the beam splitter to manipulate the interference between bunching and antibunching. Our results reveal that the temporal mode structure (multimodeness) of the quantum states shapes many-particle interference.

DOI: [10.1103/PhysRevA.100.053829](https://doi.org/10.1103/PhysRevA.100.053829)

I. INTRODUCTION

A useful tool to investigate the degree of indistinguishability of photons in quantum optics is the Hong-Ou-Mandel (HOM) interference [1]. Beyond the interest in the peculiar quantum interference itself, HOM interference is extremely important in quantum information, e.g., for the Bell-state measurement [2], for which it is used to testify to the nonlocality of entangled systems [3], and in quantum lithography [4,5]. Typically this kind of interference is studied by involving two photons in free space, though in the last years integrated quantum devices are also utilized because of their helpful features which allow one to manipulate the interference process [6,7].

However, multiphoton interference with more than two photons has attracted a lot of attention in the last two decades [8–14] since multiphoton interference is an essential and indispensable tool for boson sampling [15] and machine learning [16–19]—the first steps of future quantum computing. Moreover, multiphoton interference allows one to achieve a high-dimensional entanglement [20], overcome the standard quantum limit in interferometry [21], and create high-dimensional NOON states [22]. In addition, multiphoton interference can highlight and solve the fundamental question about the quantum-to-classical transition. In this way, a non-monotonic character of photon interference with increasing number of photons was studied in [23]. Behaviour of four-photon interference with increasing pump power was investigated in [24]. Multiphoton interference is directly connected with the multiparticle indistinguishability and the collective phase of photons [13,25]; theoretical description of multiphoton interference with a transition matrix is presented in [26].

In this paper we investigate the four-photon interference in relation to the spectral-temporal properties of the photons generated via parametric down-conversion (PDC). We show that the number of temporal modes drastically influences the interference pattern, observing a raising of the HOM dip or peak in the coincidence probability. Our analysis takes into account also different beam splitter (BS) parameters, allowing us to control the interference visibility. We show that the temporal mode structure, particularly the amount of

multimodeness, of the photon source plays a crucial role in multiphoton interference in contrast to the two-photon interference [6].

II. THEORETICAL MODEL

The type-II PDC process produces pairs of photons related by both frequency and polarization entanglement [27,28]. The Hamiltonian of the type-II PDC process can be written in terms of the joint spectral amplitude (JSA) $F(\omega_s, \omega_i)$ [29]:

$$H = \Gamma \int d\omega_s d\omega_i F(\omega_s, \omega_i) a_H^\dagger(\omega_s) a_V^\dagger(\omega_i) + \text{H.c.}, \quad (1)$$

where the indices s and i indicate the signal and idler photons, respectively, $a_{s,(i)}$ and $a_{s,(i)}^\dagger$ are the annihilation and creation operators of the signal (idler) photons, the coupling constant Γ determines the strength of interaction, and H and V label the horizontal and vertical polarization of the photons. In a periodically poled medium with the poling period Λ the JSA can be written in the form

$$F(\omega_s, \omega_i) = e^{-\frac{(\omega_s + \omega_i - \omega_p)}{2\Omega^2}} \text{sinc}\left(\frac{L}{2}\Delta k\right) e^{i\frac{L}{2}\Delta k}, \quad (2)$$

where Ω is the pump spectral bandwidth, L is the length of the PDC section, ω_p is the pump center frequency, and $\Delta k = k_p(\omega_p) - k_s(\omega_s) - k_i(\omega_i) + \frac{2\pi}{\Lambda}$ is the phase-matching condition which determines the momentum conservation of the process.

The four-photon state generated in the PDC process can be described by using the second order of the perturbation theory. Neglecting the time-ordering effects, the generated four-photon state [30–32] is

$$\begin{aligned} |\psi_{4\text{ph}}\rangle &= \frac{1}{2} \left(\int_0^t H(t') dt' \right)^2 |0\rangle \\ &= \frac{\xi^2}{2} \int_{-\infty}^{+\infty} d\omega_s d\omega_i F(\omega_s, \omega_i) a_H^\dagger(\omega_s) a_V^\dagger(\omega_i) \\ &\quad \times \int_{-\infty}^{+\infty} d\tilde{\omega}_s d\tilde{\omega}_i F(\tilde{\omega}_s, \tilde{\omega}_i) a_H^\dagger(\tilde{\omega}_s) a_V^\dagger(\tilde{\omega}_i) |0\rangle, \end{aligned} \quad (3)$$

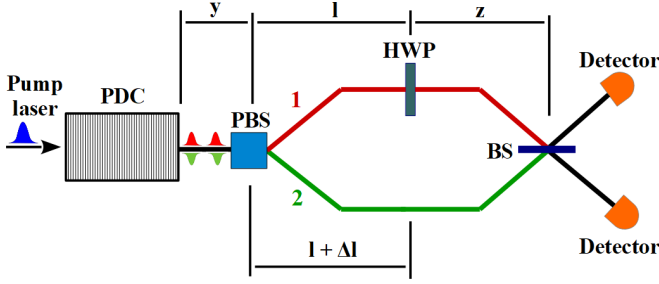


FIG. 1. Schematic setup. The type-II PDC process generates two signal-idler pairs of photons. After PBS, two horizontally polarized photons are routed to the channel 1 (red line), while two vertically polarized photons are routed to the channel 2 (green line). A half wave plate (HWP) located in the upper channel converts the horizontally polarized photons into vertically polarized ones. Due to the different group velocities of the horizontally and vertically polarized photons inside the nonlinear crystal, a time delay between the signal and idler photons is present already after the PDC section. To compensate this time delay we create an additional path increment Δl in the lower channel. In the end of the setup the four vertically polarized photons cross the BS at the same time and interfere. The interference pattern is measured at the output ports of the BS using photon number resolving detectors.

where $\omega_s, \omega_i, \tilde{\omega}_s,$ and $\tilde{\omega}_i,$ are the frequencies of the four generated photons and $\xi = \Gamma t$, where t is the time of the interaction process.

The JSA strongly depends on dispersion properties of the nonlinear material where PDC takes place [33]. For our investigation we choose a periodically poled Potassium Titanyl Phosphate (ppKTP) waveguide since this material offers flexibility in the number of Schmidt modes: a ppKTP waveguide is able to provide a quasi-single-mode PDC state, as well as the strongly multimode regime by varying the pulse duration only. Such property is more difficult to obtain in other materials (LiNbO₃, beta barium borate crystal) without filtering. To

observe the HOM interference, the incoming photons into a BS must be fully indistinguishable in all degrees of freedom: they must have the same polarization and cross the BS without any time delay. To satisfy both conditions, we consider the following setup schematically sketched in Fig. 1. In Fig. 1 the generated photons inside the PDC section are separated then by a polarization beam splitter (PBS) in two different spatial channels. The horizontally polarized photons are routed in the upper channel, and the vertically polarized photons are routed in the lower channel. A half wave plate (HWP) located in the upper channel converts the horizontally polarized photons into vertically polarized ones. Due to the different group velocities of the horizontally and vertically polarized photons inside the nonlinear crystal, a time delay between the signal and idler photons is present already after the PDC section. To compensate this time delay we create an additional path increment Δl in the lower channel. In the end of the setup the four vertically polarized photons cross the BS at the same time and interfere. The interference pattern is measured at the output ports of the BS using photon number resolving detectors.

Mathematically, all these transformations can be expressed as unitary matrices which act on the initial four-photon state. The final unitary transformation can therefore be written as a product of unitary matrices:

$$U_{\text{tot}} = \text{BS} \times \text{FP}_3 \times \text{HWP} \times \text{FP}_2 \times \text{PBS} \times \text{FP}_1, \quad (4)$$

where BS, HWP, and PBS are the matrices of the concerning elements and the matrices FP_i describe a free propagation of the light between optical elements. The output state after all transformations can be obtained after the action of the total matrix U_{tot} on the initial four-photon state. In the basis $\{a_{1H}^\dagger, a_{1V}^\dagger, a_{2H}^\dagger, a_{2V}^\dagger\}$, where the indices 1 and 2 correspond to the upper and lower channels, the output state can be represented by

$$|\psi_{\text{out}}\rangle = \frac{\xi^2}{2} \int d\omega_s d\omega_i d\tilde{\omega}_s d\tilde{\omega}_i F(\omega_s, \omega_i) F(\tilde{\omega}_s, \tilde{\omega}_i) \times U_0(\omega_s) U_{\text{tot}}^\dagger(\omega_s) \begin{pmatrix} a_{1H}^\dagger(\omega_s) \\ a_{1V}^\dagger(\omega_s) \\ a_{2H}^\dagger(\omega_s) \\ a_{2V}^\dagger(\omega_s) \end{pmatrix} \otimes U_0(\omega_i) U_{\text{tot}}^\dagger(\omega_i) \begin{pmatrix} a_{1H}^\dagger(\omega_i) \\ a_{1V}^\dagger(\omega_i) \\ a_{2H}^\dagger(\omega_i) \\ a_{2V}^\dagger(\omega_i) \end{pmatrix} \\ \otimes U_0(\tilde{\omega}_s) U_{\text{tot}}^\dagger(\tilde{\omega}_s) \begin{pmatrix} a_{1H}^\dagger(\tilde{\omega}_s) \\ a_{1V}^\dagger(\tilde{\omega}_s) \\ a_{2H}^\dagger(\tilde{\omega}_s) \\ a_{2V}^\dagger(\tilde{\omega}_s) \end{pmatrix} \otimes U_0(\tilde{\omega}_i) U_{\text{tot}}^\dagger(\tilde{\omega}_i) \begin{pmatrix} a_{1H}^\dagger(\tilde{\omega}_i) \\ a_{1V}^\dagger(\tilde{\omega}_i) \\ a_{2H}^\dagger(\tilde{\omega}_i) \\ a_{2V}^\dagger(\tilde{\omega}_i) \end{pmatrix} |0\rangle, \quad (5)$$

where $U_0(\omega_s)$ and $U_0(\omega_i)$ are the initial condition matrices [34]. The output state Eq. (5) can be modified and written in the basis $|m, n\rangle$ with the probability amplitudes $C_{m,n}(\Delta l, \tau, L)$, where m indicates the number of photons in the upper channel and n indicates the number of photons in the lower channel:

$$|\psi_{\text{out}}\rangle = \int d\omega_s d\omega_i d\tilde{\omega}_s d\tilde{\omega}_i [C_{22}(\Delta l, \tau, L)|2, 2\rangle + C_{31}(\Delta l, \tau, L)(|3, 1\rangle + |1, 3\rangle) + C_{40}(\Delta l, \tau, L)(|4, 0\rangle + |0, 4\rangle)]. \quad (6)$$

By using the final state Eq. (6), we can calculate the expectation values of the simultaneous positive-operator valued measures, which correspond to the measured coincidence probability at the detectors:

$$P_{22}(\Delta l, \tau, L) = \int d\omega_b d\omega_c d\tilde{\omega}_b d\tilde{\omega}_c \left| \langle 0 | \frac{1}{\sqrt{2!}\sqrt{2!}} d_1(\omega_b) d_2(\omega_c) d_1(\tilde{\omega}_b) d_2(\tilde{\omega}_c) | \tilde{\psi}_{\text{out}} \rangle \right|^2, \quad (7)$$

$$P_{31}(\Delta l, \tau, L) = \int d\omega_b d\omega_c d\tilde{\omega}_b d\tilde{\omega}_c \langle 0 | \frac{1}{\sqrt{3!}} d_1(\omega_b) d_1(\omega_c) d_1(\tilde{\omega}_b) d_2(\tilde{\omega}_c) |\tilde{\psi}_{\text{out}}\rangle|^2, \quad (8)$$

$$P_{40}(\Delta l, \tau, L) = \int d\omega_b d\omega_c d\tilde{\omega}_b d\tilde{\omega}_c \langle 0 | \frac{1}{\sqrt{4!}} d_1(\omega_b) d_1(\omega_c) d_1(\tilde{\omega}_b) d_1(\tilde{\omega}_c) |\tilde{\psi}_{\text{out}}\rangle|^2, \quad (9)$$

where d_1 and d_2 are the annihilation operators of the detectors placed in the upper and the lower channels, respectively; $\omega_b, \omega_c, \tilde{\omega}_b$, and $\tilde{\omega}_c$ are the frequencies of the detectors; and $|\tilde{\psi}_{\text{out}}\rangle = |\psi_{\text{out}}\rangle / \langle \psi_{\text{out}} | \psi_{\text{out}} \rangle$ is the normalized output state. Equations (7)–(9) present the probability P_{mn} to detect m photons in the upper channel and n photons in the lower channel, respectively.

III. RESULTS AND DISCUSSION

A. Experiment

To study the impact of time-frequency correlations of the state on the four-photon interference, we employ an engineered, programmable PDC source. Our source is an 8-mm-long waveguide in KTP, engineered to the symmetric group velocity matching condition, which allows us to flexibly control the frequency correlation between signal and idler photons by modulating the pump pulses only [35,36]. We pump the source with ultrashort pulses out of a Ti:Sa oscillator, followed by a pulse shaper. The pulse shaper is based on a spatial light modulator in a $4f$ setup, which allows us to shape the spectral amplitude and phase of pump pulses. With this configuration we can have pulses with time bandwidths ranging from 0.3 to 40 ps. To choose a pump power, we found an operational point to have enough detection counts from four photons while keeping the contribution from higher photon numbers small. We drive the source with a pump pulse energy of approximately 6.5 pJ, which generates a PDC mean photon number of 0.02 per pulse, and where the probability of generating four photons is about 50 times bigger than six photons. Further details of the experimental setup are given in Fig. 2 [35,37].

In this paper we consider three PDC states (A, B, and C), generated by pump pulses with bandwidths of 0.14, 1.29, and 6.62 ps, as summarized in Table I. To shape the temporal profile of the pump field in the case of states A and B, we simply increase the pulse duration and carve out the corresponding spectral amplitude with a constant spectral phase. This approach works pretty well for short pulse durations but for long pulse duration results in significantly small pulse energies which, in turn, reduce the probability of generating PDC photons. For this reason, in the case of state C we take an alternative method; we use the same spectral amplitude as in case A but with a quadratic spectral phase related to the constant $D = 1.9 \text{ ps}^2$. This additional phase modifies the JSA as follows:

$$\tilde{F}(\omega_s, \omega_i) = F(\omega_s, \omega_i) e^{iD(\omega_s + \omega_i - \omega_p)^2}. \quad (10)$$

To characterize the joint spectral intensity (JSI) $|F(\omega_s, \omega_i)|^2$ of PDC states, we employ a time-of-flight spectrometer with a resolution of 0.1 nm, measuring twofold coincidences between signal and idler spectrometers [38].

In the first column of Fig. 3 we plot measured JSIs of three PDC states. Since the JSI does not contain any information about the spectral phase, the JSIs of states A and C are essentially identical. State B, however, features a strong frequency anticorrelation. The second column of Fig. 3 presents theoretically calculated spectral amplitude and phase of the considered JSAs; it is clearly seen that states A and C are completely different due to the phase.

To find a better understanding of our experiment, it would be helpful to translate the spectral representation to temporal description by means of Fourier transform, since the HOM interference shows an indistinguishability of photons with the same polarization and mode structure in time:

$$F(t_s, t_i) = \int d\omega_s d\omega_i F(\omega_s, \omega_i) e^{i(\omega_s t_s + \omega_i t_i)}. \quad (11)$$

The absolute value of the joint time amplitude (JTA), Eq. (11), is depicted in the third column of Fig. 3. In these plots, it is clearly seen that the temporal correlation between signal and idler photons, the multimodeness in the state, is increasing from state A to B and to C. Despite distinctively different pump pulse bandwidths, the width of the two-photon HOM interference is mainly determined by the fixed crystal length and thus nearly identical for all three states, as experimentally shown in the fourth column of Fig. 3. This independence of

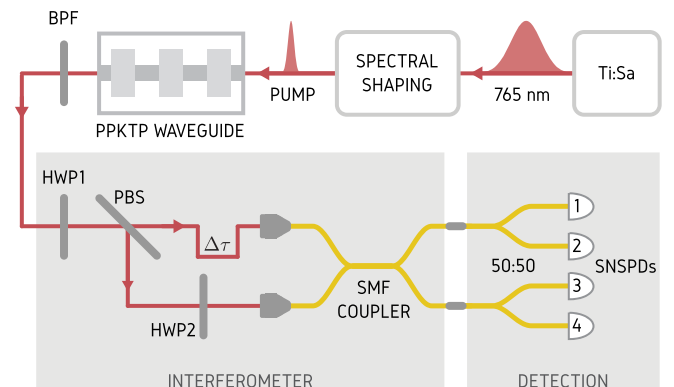


FIG. 2. Experimental setup. A femtosecond titanium:sapphire (Ti:Sa) oscillator with repetition rate of 80 MHz is used to pump a PPKTP waveguide designed for type-II PDC. For spectral shaping of the pump, we use a spatial light modulator (SLM) in a folded $4f$ setup to shape the desired spectral amplitude and phase. An 8-nm-wide bandpass filter (BPF) centered at 1532 nm was used to block the pump and phase-matching side lobes. The orthogonally polarized PDC photons were sent to the interferometer setup, where we used a polarizing beamsplitter (PBS), a half wave plate (HWP), and an adjustable time delay stage $\Delta\tau$ to control the interference. Then the photons were sent to a single-mode fiber coupler with an adjustable coupling ratio where interference occurs. Each output port of the fiber coupler is then connected to a balanced fiber splitter followed by superconducting nanowire single photon detectors (SNSPD).

TABLE I. Overview of studied PDC states. Δ denotes the standard deviation; V denotes the visibility and ΔL denotes the standard deviation of $P_{1,1}$ interference, calculated with a Gaussian fit function to the theory and experiment.

	State A	State B	State C
Pump field amplitude setting			
$\Delta\lambda_{\text{pump}}$ (nm)	1.8	0.2	1.8
$\Delta\omega_{\text{pump}}$ (THz)	3.479	0.386	3.44
D (ps ²)	0	0	1.9
Δt_{pump} (ps)	0.14	1.29	6.62
Correlation function and Schmidt number			
$g^{(2)}(\tau = 0)$	1.897 ± 0.011	1.233 ± 0.010	1.108 ± 0.003
$K = \frac{1}{g^{(2)} - 1}$	1.11	4.29	9.25
$P_{1,1}$ interference			
$V_{\text{th.}}$ (%)	92.7	100.0	92.7
$V_{\text{exp.}}$ (%)	90.7 ± 0.5	92.7 ± 0.7	90.2 ± 0.8
$\Delta L_{\text{th.}}$ (mm)	0.368	0.341	0.368
$\Delta L_{\text{exp.}}$ (mm)	0.381 ± 0.003	0.358 ± 0.004	0.373 ± 0.005

the two-photon HOM interference on pump pulse duration is a consequence of a special dispersion characteristic of our PDC source which has been reported in the past [30,39].

The visibility of the HOM dip, on the other hand, is governed by the symmetry of JSA around the main diagonal $\lambda_s = \lambda_i$: for the nonsymmetrical JSA even for zero time delay the probability to observe two photons in two channels is not zero.

To characterize the Schmidt number $K = \frac{1}{g^{(2)} - 1}$ of PDC states, we measure the unheralded second-order correlation function $g^{(2)}(\tau = 0)$ [40]. The $g^{(2)}$ measurement probes the photon number statistics of signal or idler photons, where a single-mode PDC state shows $g^{(2)} = 2$ and a highly multimode state gives $g^{(2)} = 1$. As shown in Table I, state A is nearly single mode while states B and C have an increasing amount of multimodeness.

B. Balanced BS

In this section, we investigate the four-photon interference using the aforementioned three PDC states. In the first part of our analysis, we use a balanced BS, i.e., having the same values for the reflection and transmission coefficients. The probabilities P_{mn} to detect m photons in the upper channel and n photons in the lower channel described by Eqs. (7)–(9) are plotted in Fig. 4.

We can clearly observe that by varying the pump pulse duration the four-photon HOM interference is modified considerably, unlike what was expected in the case of two-photon interference, seen in Fig. 3. Such behavior reflects the

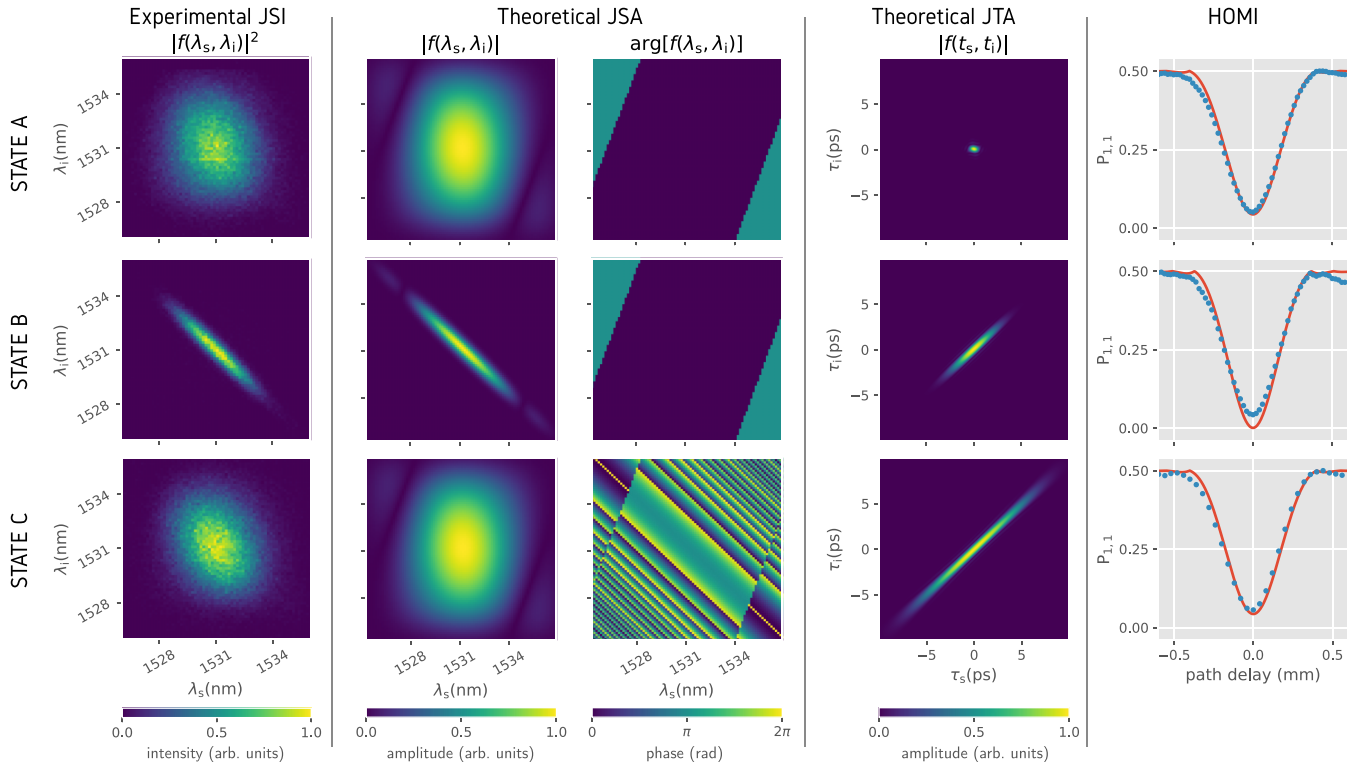


FIG. 3. Spectral-temporal properties of considered PDC states: state A is nearly decorrelated, state B is standard frequency anticorrelated, and state C has spectral phase anticorrelations from a strongly chirped pump. The first column presents measured joint spectral intensity (JSI), which contains no information about the spectral phase. The second column depicts the absolute value and the phase of theoretical joint spectral amplitudes (JSAs). The third column shows the absolute value of theoretical joint temporal amplitudes (JTAs). The fourth column shows the calculated (red solid line) and measured (blue dots) two-photon Hong-Ou-Mandel interference (HOMI), with error bars smaller than the dots. Experimental points on $P_{1,1}$ correspond to twofold coincidences between detectors 1 and 3, with maximum count rates of 1 590 426, 1 583 615, and 1 675 548 per 60 s for states A, B, and C, respectively.

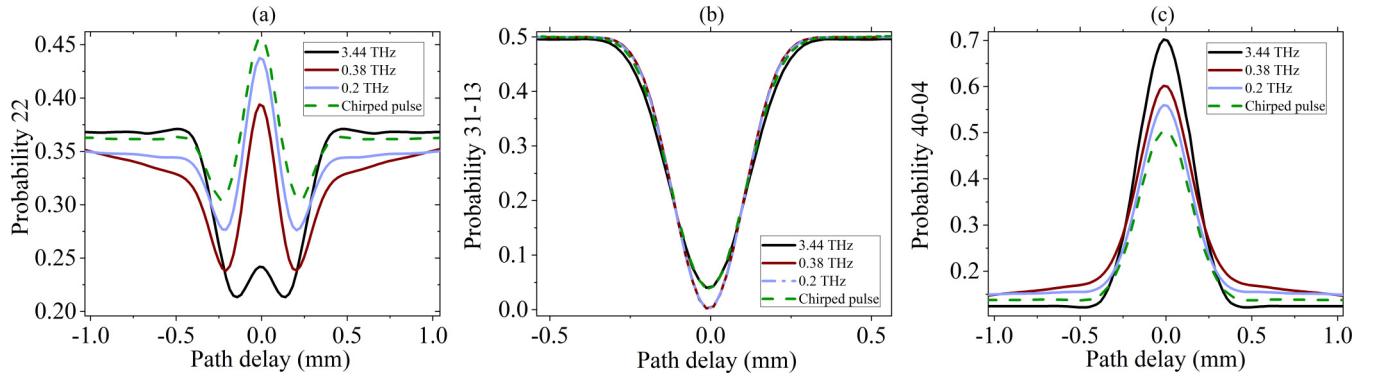


FIG. 4. Theoretical coincidence probabilities to detect: (a) two photons per channel, (b) three photons in one channel and one photon in the other channel, and (c) four photons in one channel for different pump spectral bandwidths [states A, B, and C are presented by black, red (dark gray), and dashed green curves, respectively].

complexity of multiphoton interference and can be explained by the number of Schmidt modes [41] in the PDC state. Indeed, the black line in Fig. 4 corresponds to the quasi-single-mode case, state A, with the Schmidt number $K = 1.1$ and near circular JTA. Increasing the pump temporal duration, states B and C, results in a higher number of modes, which leads to a stronger antibunching effect at zero time delay which is reflected in growing of the P_{22} probability.

Simultaneously, for zero time delay under the assumption of symmetrical JSA, i.e., $F(\omega_s, \omega_i) = F(\omega_i, \omega_s)$, the P_{22} and $P_{40} = 1 - P_{22}$ probabilities can be calculated analytically using the Schmidt decomposition of JSA: $F(\omega_s, \omega_i) = \sum_n \sqrt{\Lambda_n} u_n(\omega_s) v_n(\omega_i)$, where Λ_n are eigenvalues and u_n and v_n are eigenfunctions of the Schmidt decomposition [41] (see the Appendix):

$$P_{22} = \frac{1}{2 + 2 \sum_n \Lambda_n^2}. \quad (12)$$

This means that P_{22} can be varied from $P_{22} = 1/4$ in the decorrelated single-mode regime to $P_{22} = 1/2$ in the multimode case, when strong time correlations between the signal and idler photons take place. This relation between the degree of multimodeness, which is characterized by the Schmidt number $K = 1/\sum_n \Lambda_n^2$, and antibunching properties of light can be observed in the case of multiphoton interference only. The last is highly relevant for any quantum networks dealing

with multimode many-particle states like boson sampling. An obtained link between the degree of correlations and the interference pattern is quite general: a similar dependence of P_{22} probability on the degree of polarization entanglement was observed in [42]. The obtained results show that the number of temporal modes of the light and the degree of time correlations can be estimated by using four-photon interference. It is important to note that there are no analogous variations in the case of two-photon interference. Only by adding additional elements, for example, four slits, can similar modifications of the interference pattern be found [43].

In the case of state C the JSI is the same as in the quasi-single-mode case A, but due to the quadratic phase of the pump pulse their JTAs are completely different (see Fig. 3); the last leads to different interference patterns. However, for states of light with the same JTAs the coincidence probabilities are identical since behavior of multiphoton interference is determined by temporal properties of light. For example, the interference patterns in case C and in the case of the small pump spectral bandwidth 0.2 THz are close to each other [Fig. 4(b), dashed green and blue (light gray) lines] and show the multimodeness of light.

Moreover, in the four-photon case the symmetry of JSA is very important because it strongly affects the P_{31} probability. In particular, in cases A and C the JSA is not fully symmetrical around the main diagonal, which leads to the

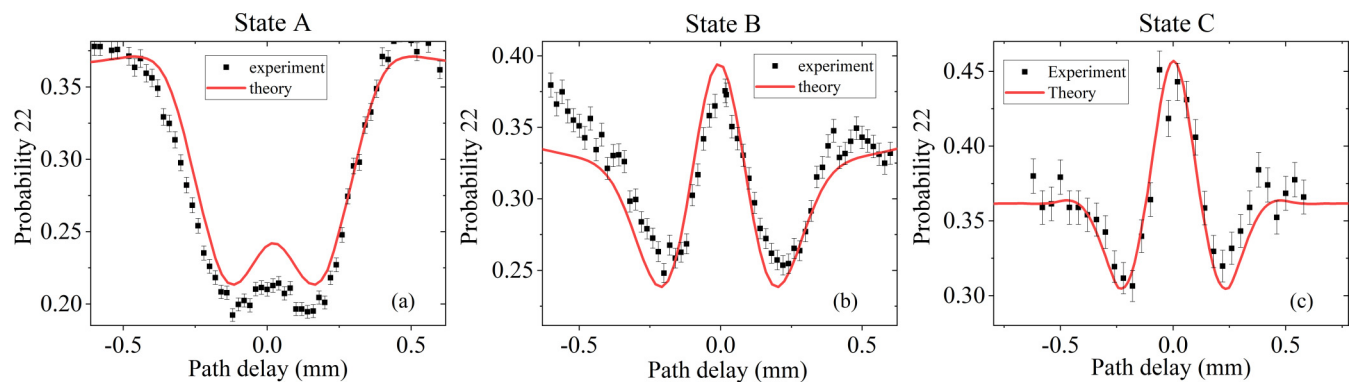


FIG. 5. Theoretical and experimental P_{22} probabilities for states A, B, and C. Experimental points correspond to maximum counting rates of 3761, 2127, and 2309 per 60 s for states A, B, and C, respectively.

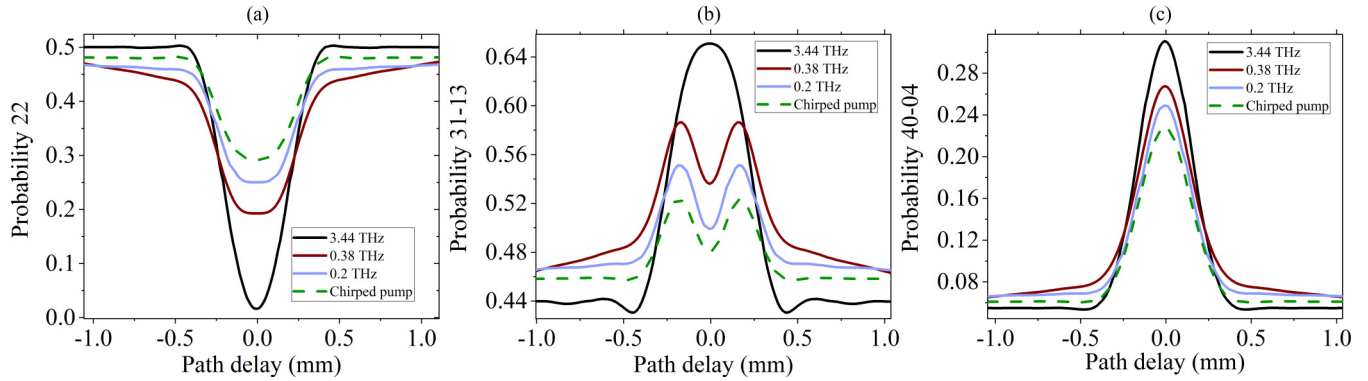


FIG. 6. Unbalanced BS configuration. Theoretical coincidence probabilities to detect: (a) two photons per channel, (b) three photons in one channel and one photon in the other channel, and (c) four photons in one channel for different pump spectral bandwidths [states A, B, and C in black, red (dark gray), and dashed green, respectively].

nonzero P_{31} probability even for zero time delay [Fig. 4(b), black and green curves]. Nevertheless, by decreasing the pump spectral bandwidth the JSA becomes more symmetrical with respect to the signal-idler variables exchange, case B, and as a consequence P_{31} vanishes when $\Delta l = 0$ [red (dark gray) line in Fig. 4(b)].

To justify our theoretical analysis we built the experimental setup as sketched in Fig. 2. Four detectors in the end of the setup allow us to analyze the four-photon interference. The comparison between measured coincidence probabilities and theoretical calculations are illustrated in Fig. 5 by black dots and red curves, respectively.

C. Unbalanced BS

A balanced beam splitter, i.e., a beam splitter having the same values for both transmission and reflection coefficients, is a fundamental tool in the two-photon interference scenario, since it allows one to inhibit the probability to measure two photons in different channels. In the four-photon scenario, a balanced BS is able to annul the P_{31} probability but cannot erase the P_{22} probability. That is why it is also interesting to take into account other values of the BS parameters, which allow one to inhibit the output state with two photons in both channels and provide an analogy with the two-photon

interference. The values of the transmission and reflection coefficients of the BS which erase the P_{22} probability for zero time delay in the single-mode (plane-wave) case are $(3 \pm \sqrt{3})/6$ [44].

In Fig. 6 one can observe the behavior of the P_{mn} probabilities for the different JSAs depicted in Fig. 3. As it is clearly seen, using the unbalanced BS we can inhibit drastically the P_{22} by imposing a circular JSA [black curve in Fig. 6(a)]. Nevertheless, it is not possible to annul the P_{22} totally since the JSA is not perfectly circular. With increasing number of modes, P_{22} grows. It is worth observing that the P_{31} probability, which shows a dip using a balanced BS, transforms to the broad peak in the unbalanced case, which is a consequence of the unbalanced BS. The comparison with the experimental data is shown in Fig. 7.

In the case of the unbalanced BS and taking the single-mode state, the P_{22} probability is similar to the typical two-photon HOM dip and we can therefore compare such case with the two-photon interference (the P_{11} probability) by using the same parameters but the balanced BS. The comparison is presented in Fig. 8, where one can observe that the minimum points of the dips in P_{22} and P_{11} cases are close to each other. However, P_{22} is 7.5% broader than P_{11} , which indicates a larger range of indistinguishability of four photons due to the unbalanced BS.

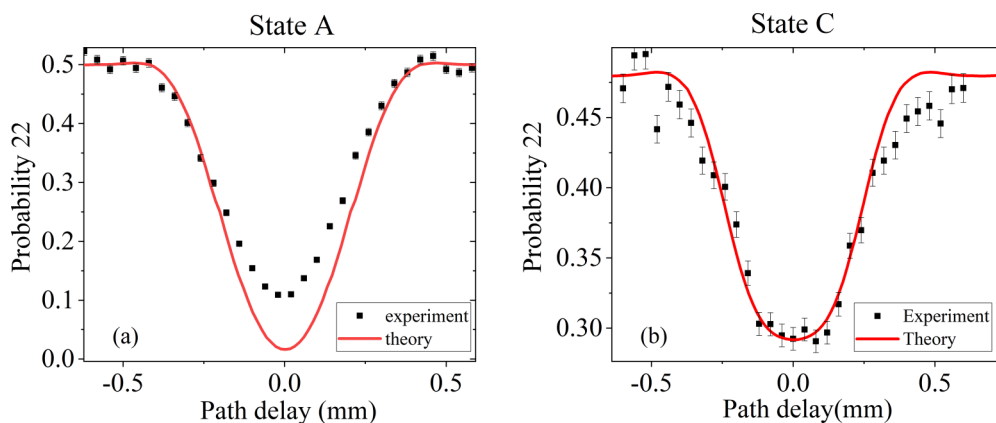


FIG. 7. Theoretical and experimental P_{22} probabilities for states A and C in the unbalanced BS configuration. Experimental points correspond to maximum counting rates of 5128 and 2094 per 60 s for states A and C, respectively.

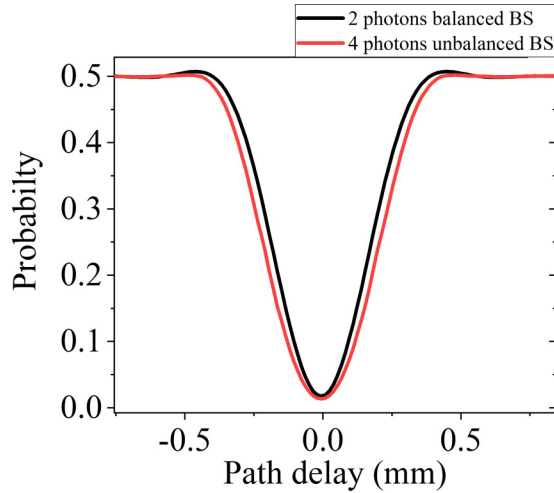


FIG. 8. The two-photon HOM dip with a balanced BS and the four-photon HOM dip with an unbalanced BS in the single-mode regime: the pulse duration is 0.29 ps.

IV. CONCLUSION

The four-photon Hong-Ou-Mandel interference was investigated by using different mode content of the PDC source. It was observed that the HOM profiles depend strictly on the parameters of the source in terms of both the number of Schmidt modes and the symmetry of the JSA. An antibunching behavior in the interference pattern of four-photon interference is directly connected with the number of temporal modes (multimodeness) in the system and becomes more pronounced with increasing the Schmidt parameter. Such behavior can be observed in the case of multiphoton interference only.

The number of modes was modified by varying the pump spectral bandwidth and by using a chirped pump pulse. The last case with artificial creation of multimodeness by adding a quadratic spectral phase allows one to increase significantly the number of modes without decreasing the pulse energy and maintaining the same signal-idler spectrum.

Also we demonstrated that it is possible to change drastically the shape of the HOM curves by varying the transmission and reflection parameters of the beam splitter. It was shown that with a specific choice of such parameters the four-photon interference can be similar to the two-photon interference but with a larger range of photon indistinguishability and better stability to the asymmetry of JSA.

Presented results illuminate features of multiphoton interference using a real multimode photon source and open an avenue for further investigation of multiphoton interference and its implementation into quantum networks and quantum computing algorithms based on photonic structures.

ACKNOWLEDGMENTS

We acknowledge the financial support of the Deutsche Forschungsgemeinschaft via Grant No. TRR 142/1, Project No. CO2. P.R.Sh. thanks the state of North Rhine-Westphalia for support by the *Landesprogramm für geschlechtergerechte Hochschulen*.

APPENDIX: RELATION BETWEEN P_{22} AND THE NUMBER OF MODES

In this Appendix we show how the peak in P_{22} at zero time delay depends on the number of Schmidt modes of the source. At zero time delay, the expression for P_{22} probability can be drastically reduced due to the symmetry of the JSA with respect to the main diagonal:

$$P_{22} = \frac{\int d\omega_b d\omega_c d\tilde{\omega}_b d\tilde{\omega}_c F(\omega_c, \omega_d) F(\tilde{\omega}_c, \tilde{\omega}_d) F^*(\omega_d, \omega_c) F^*(\tilde{\omega}_d, \tilde{\omega}_c)}{2 + 2 \int d\omega_b d\omega_c d\tilde{\omega}_b d\tilde{\omega}_c F(\omega_c, \omega_d) F(\tilde{\omega}_c, \tilde{\omega}_d) F^*(\omega_d, \tilde{\omega}_c) F^*(\tilde{\omega}_d, \omega_c)}. \quad (\text{A1})$$

The integration in the numerator tends to unity due to the normalization of the JSA. To calculate the expression in the denominator it is helpful to perform the Schmidt decomposition of the JSAs:

$$\begin{aligned} & \int d\omega_b d\omega_c d\tilde{\omega}_b d\tilde{\omega}_c F(\omega_c, \omega_d) F(\tilde{\omega}_c, \tilde{\omega}_d) F^*(\omega_d, \tilde{\omega}_c) F^*(\tilde{\omega}_d, \omega_c) \\ &= \sum_{\alpha\beta\gamma\delta} \sqrt{\Lambda_\alpha \Lambda_\beta \Lambda_\gamma \Lambda_\delta} \int d\omega_b d\omega_c d\tilde{\omega}_b d\tilde{\omega}_c u_\alpha(\omega_c) u_\beta(\tilde{\omega}_c) u_\gamma^*(\omega_d) u_\delta^*(\tilde{\omega}_d) v_\alpha(\omega_c) v_\beta(\tilde{\omega}_c) v_\gamma^*(\omega_d) v_\delta^*(\tilde{\omega}_d), \end{aligned} \quad (\text{A2})$$

where parameters Λ_n and functions $u_n(\omega)$ and $v_n(\omega)$ are Schmidt eigenvalues and eigenfunctions, respectively. Due to the symmetry of JSA we can assume $u \equiv v$. Using the orthonormalization of the Schmidt-mode basis, the integral in the denominator can be taken and the final P_{22} probability at zero time delay, Eq. (12), can be obtained. As predicted theoretically and confirmed experimentally, such probability at zero time delay depends strictly on the number of Schmidt modes, defined as

$K = 1/(\sum_\alpha \Lambda_\alpha^2)$. When the JTA is extremely narrow, the number of Schmidt modes increases. Such situation leads to the bunching behavior observed both theoretically and experimentally in Figs. 4 and 5, respectively. With increasing the number of Schmidt modes either via the pump spectral bandwidth or via the quadratic phase chirped pump, the system acquires a higher degree of entanglement, and, as a consequence of that, an antibunching peak is observed.

- [1] C.-K. Hong, Z.-Y. Ou, and L. Mandel, *Phys. Rev. Lett.* **59**, 2044 (1987).
- [2] K. Mattle, H. Weinfurter, P. G. Kwiat, and A. Zeilinger, *Phys. Rev. Lett.* **76**, 4656 (1996).
- [3] J. R. Torgerson, D. Branning, C. H. Monken, and L. Mandel, *Phys. Lett. A* **204**, 323 (1995).
- [4] E. M. Nagasako, S. J. Bentley, R. W. Boyd, and G. S. Agarwal, *Phys. Rev. A* **64**, 043802 (2001).
- [5] A. N. Boto, P. Kok, D. S. Abrams, S. L. Braunstein, C. P. Williams, and J. P. Dowling, *Phys. Rev. Lett.* **85**, 2733 (2000).
- [6] P. R. Sharapova, K. H. Luo, H. Herrmann, M. Reichelt, C. Silberhorn, and T. Meier, *Phys. Rev. A* **96**, 043857 (2017).
- [7] Y. L. Lim and A. Beige, *New J. Phys.* **7**, 155 (2005).
- [8] M. C. Tichy, M. Tiersch, F. Mintert, and A. Buchleitner, *New J. Phys.* **14**, 093015 (2012).
- [9] Z. Y. Ou, J.-K. Rhee, and L. J. Wang, *Phys. Rev. A* **60**, 593 (1999).
- [10] A. F. Abouraddy, T. M. Yarnall, and G. Di Giuseppe, *Phys. Rev. A* **87**, 062106 (2013).
- [11] Z. Y. Ou, J.-K. Rhee, and L. J. Wang, *Phys. Rev. Lett.* **83**, 959 (1999).
- [12] S. Agne, T. Kauten, J. Jin, E. Meyer-Scott, J. Z. Salvail, D. R. Hamel, K. J. Resch, G. Weihs, and T. Jennewein, *Phys. Rev. Lett.* **118**, 153602 (2017).
- [13] A. J. Menssen, A. E. Jones, B. J. Metcalf, M. C. Tichy, S. Barz, W. S. Kolthammer, and I. A. Walmsley, *Phys. Rev. Lett.* **118**, 153603 (2017).
- [14] T. Giordani, F. Flamini, M. Pompili, N. Viggianiello, N. Spagnolo, A. Crespi, R. Osellame, N. Wiebe, M. Walschaers, A. Buchleitner *et al.*, *Nat. Photonics* **12**, 173 (2018).
- [15] M. Bentivegna, N. Spagnolo, C. Vitelli, F. Flamini, N. Viggianiello, L. Latmiral, P. Mataloni, D. J. Brod, E. F. Galvão, A. Crespi *et al.*, *Sci. Adv.* **1**, e1400255 (2015).
- [16] Y. Shen, N. C. Harris, S. Skirlo, M. Prabhu, T. Baehr-Jones, M. Hochberg, X. Sun, S. Zhao, H. Larochelle, D. Englund *et al.*, *Nat. Photonics* **11**, 441 (2017).
- [17] T. W. Hughes, M. Minkov, Y. Shi, and S. Fan, *Optica* **5**, 864 (2018).
- [18] A. N. Tait, T. F. de Lima, E. Zhou, A. X. Wu, M. A. Nahmias, B. J. Shastri, and P. R. Prucnal, *Sci. Rep.* **7**, 7430 (2017).
- [19] F. Flamini, N. Spagnolo, and F. Sciarrino, *Quantum Sci. Technol.* **4**, 024008 (2019).
- [20] P. Walther, J.-W. Pan, M. Aspelmeyer, R. Ursin, S. Gasparoni, and A. Zeilinger, *Nature (London)* **429**, 158 (2004).
- [21] T. Nagata, R. Okamoto, J. L. O'Brien, K. Sasaki, and S. Takeuchi, *Science* **316**, 726 (2007).
- [22] I. Afek, O. Ambar, and Y. Silberberg, *Science* **328**, 879 (2010).
- [23] Y.-S. Ra, M. C. Tichy, H.-T. Lim, O. Kwon, F. Mintert, A. Buchleitner, and Y.-H. Kim, *Proc. Natl. Acad. Sci. USA* **110**, 1227 (2013).
- [24] O. Cosme, S. Pádua, F. A. Bovino, A. Mazzei, F. Sciarrino, and F. De Martini, *Phys. Rev. A* **77**, 053822 (2008).
- [25] Z. Ou, *Phys. Rev. A* **72**, 053814 (2005).
- [26] M. Tillmann, S.-H. Tan, S. E. Stoeckl, B. C. Sanders, H. de Guise, R. Heilmann, S. Nolte, A. Szameit, and P. Walther, *Phys. Rev. X* **5**, 041015 (2015).
- [27] H. Weinfurter and M. Zukowski, *Phys. Rev. A* **64**, 010102(R) (2001).
- [28] J. C. Howell, A. Lamas-Linares, and D. Bouwmeester, *Phys. Rev. Lett.* **88**, 030401 (2002).
- [29] N. Quesada and J. E. Sipe, *Phys. Rev. A* **90**, 063840 (2014).
- [30] V. Ansari, B. Brecht, G. Harder, and C. Silberhorn, *arXiv:1404.7725*.
- [31] H. D. Riedmatten, V. Scarani, I. Marcikic, A. Acín, W. Tittel, H. Zbinden, and N. Gisin, *J. Mod. Opt.* **51**, 1637 (2004).
- [32] B.-S. Shi and A. Tomita, *J. Mod. Opt.* **53**, 1003 (2006).
- [33] K. Kato and E. Takaoka, *Appl. Opt.* **41**, 5040 (2002).
- [34] P. Sharapova, K. Luo, H. Herrmann, M. Reichelt, T. Meier, and C. Silberhorn, *New J. Phys.* **19**, 123009 (2017).
- [35] G. Harder, V. Ansari, B. Brecht, T. Dirmeyer, C. Marquardt, and C. Silberhorn, *Opt. Express* **21**, 13975 (2013).
- [36] V. Ansari, J. M. Donohue, B. Brecht, and C. Silberhorn, *Optica* **5**, 534 (2018).
- [37] V. Ansari, J. M. Donohue, M. Allgaier, L. Sansoni, B. Brecht, J. Roslund, N. Treps, G. Harder, and C. Silberhorn, *Phys. Rev. Lett.* **120**, 213601 (2018).
- [38] M. Avenhaus, A. Eckstein, P. J. Mosley, and C. Silberhorn, *Opt. Lett.* **34**, 2873 (2009).
- [39] O. Kuzucu, M. Fiorentino, M. A. Albota, F. N. C. Wong, and F. X. Kaertner, *Phys. Rev. Lett.* **94**, 083601 (2005).
- [40] A. Christ, K. Laiho, A. Eckstein, K. N. Cassemiro, and C. Silberhorn, *New J. Phys.* **13**, 033027 (2011).
- [41] C. K. Law, I. A. Walmsley, and J. H. Eberly, *Phys. Rev. Lett.* **84**, 5304 (2000).
- [42] K. Tsujino, H. F. Hofmann, S. Takeuchi, and K. Sasaki, *Phys. Rev. Lett.* **92**, 153602 (2004).
- [43] M. V. Fedorov, A. A. Sysoeva, S. V. Vintskevich, and D. A. Grigoriev, *Phys. Rev. A* **98**, 013850 (2018).
- [44] B. Liu, F. Sun, Y. Gong, Y. Huang, G. Guo, and Z. Ou, *Opt. Lett.* **32**, 1320 (2007).